J. Fluid Mech. (2007), *vol.* 579, *pp.* 347–371. © 2007 Cambridge University Press
doi:10.1017/S0022112007005319 Printed in the United Kingdom

A spherical-cap bubble moving at terminal velocity in a viscous liquid

JAMES Q. FENG
Cardiovascular R & D, Boston Scientific Corporation, Three Scimed Place C-150,
Maple Grove, MN 55311, USA
james.feng@bsci.com

(Received 5 September 2006 and in revised form 24 November 2006)

The nonlinear Navier–Stokes equations governing steady, laminar, axisymmetric flow past a deformable bubble are solved by the Galerkin finite-element method simultaneously with a set of elliptic partial differential equations governing boundary-fitted mesh. For Reynolds number $20 \leqslant Re \leqslant 500$, numerical solutions of spherical-cap bubbles are obtained at capillary number $Ca = 1$. Increasing Ca to 2 leads to a highly curved, cusp-like bubble rim that seems to correspond to skirt formation. The computed steady, axisymmetric spherical-cap bubbles with closed, laminar wakes compare reasonably with the available experimental results, especially for $Re \leqslant 100$. By exploring the parameter space (for $Re \leqslant 200$), a sufficient condition for steady axisymmetric solutions of bubbles with the spherical-cap shape is found to be roughly $Ca > 0.4$. The basic characteristics of spherical-cap bubbles of $Ca \geqslant 0.5$, for a given $Re \geqslant 50$, are found to be almost independent of the value of Ca (or Weber number $We \equiv Re\,Ca$). At a fixed $Re \geqslant 50$, continuation by increasing Ca (or We) from a spherical bubble solution cannot lead to solutions of spherical-cap bubbles, but rather to a turning point at We slightly greater than 10 where the solution branch folds back to reduced values of Ca (or We). Yet continuation by reducing Ca (or We) from a spherical-cap bubble solution cannot arrive at a spherical bubble solution for $Re \geqslant 50$, but rather at solutions with bubbles having more complicated shapes such as a sombrero, etc. Without thorough examinations of the solution stability, multiple steady axisymmetric solutions are shown to exist in the parameter space for a given set of parameters.

1. Introduction

The behaviour of a gas bubble moving in a viscous liquid has been investigated by numerous authors as a fundamental subject of fluid mechanics, because of its relevance to various practical applications as well as its ubiquity in our everyday life. An extensive literature review may be found in the article of Wegener & Parlange (1973) and citations referred to therein. Driven by the buoyancy force, a bubble is often experimentally observed to move at a constant terminal velocity after an initial acceleratory transient (Haberman & Morton 1953; Batchelor 1967; Harper 1972; Wegener & Parlange 1973; Clift, Grace & Weber 1978). Smaller bubbles moving at lower terminal velocities exhibit nearly spherical shapes due to relatively strong surface tension effects. With increasing bubble size, the terminal velocity increases and the bubble shape becomes increasingly oblate. Large bubbles have been found to take an apparently ‘spherical cap’ shape, often with turbulent flow in the wake, as first studied by Davies & Taylor (1950). Steady spherical-cap bubbles with laminar wakes of toroidal vortices were observed for $Re < 200$ (e.g., Slaughter & Wraith 1968; Wegener & Parlange 1973; Bhaga & Weber 1981).

With the deformable free surface, a gas bubble moving in a viscous liquid poses an intrinsically nonlinear problem that is intractable with conventional mathematical techniques. Early theoretical studies were limited to cases of very small bubble deformations either at high Reynolds number (Moore 1959; 1965) or at low Reynolds number (Taylor & Acrivos 1964; Brignell 1973). The potential-flow analysis of spherical-cap bubbles by Davies & Taylor (1950) and Collins (1966) yielded a relationship between the bubble terminal velocity and the radius of curvature of the front part of bubble surface, with the spherical-cap shape assumed *a priori* and both fluid viscosity and surface tension neglected. The terminal velocity formula of Davies & Taylor was extended by Joseph (2003) to include the effects of fluid viscosity and surface tension by applying the theory of viscous potential flow that assumes zero vorticity. Some semi-empirical models were also provided in the literature (Parlange 1969).

The advent of modern high-speed computers has enabled development of various numerical methods for ‘self-consistently’ solving complicated nonlinear free-boundary problems such as moving bubbles in viscous liquids. By solving the Navier–Stokes equations in boundary-fitted, orthogonal coordinates with a finite-difference scheme, Ryskin & Leal (1984) and Christov & Volkov (1985) were able to compute the steady-state flow field and bubble shape over a range of Reynolds number and Weber number. For cases of Reynolds number $Re \leqslant 20$, the computed axisymmetric shape of the bubble changes from spherical to oblate to spherical-cap with increasing Weber number We. At higher Reynolds numbers (e.g. $Re = 100$ and 200), ‘disk-like’ and ‘saucer-like’ steady bubble shapes were predicted at $We \approx 10$. Although their numerical technique did not allow them to compute solutions for $We > 10$ when $Re \geqslant 50$, Ryskin & Leal (1984) commented that the branch of solutions they obtained does not seem likely to revert from the saucer-like bubble shape to the experimentally observed spherical-cap bubble shape at larger We. The possibility of the onset of ‘shape instabilities’ was suggested, implying the non-existence of steady axisymmetric bubble shapes above some critical Weber number.

Using a modified volume-of-fluid method incorporating the surface tension effect, Chen *et al.* (1999) computed transient development of a bubble rising in a viscous liquid with results showing spherical-cap shapes for $Re < 50$ that compare reasonably with the experimental photographs of Bhaga & Weber (1981). With a coupled level set/volume-of-fluid method, Ohta *et al.* (2005) also computed some cases of spherical-cap bubbles showing reasonable comparison with a few experimental images for $Re < 50$. In studying initial condition effects on axisymmetric bubble evolution based on transient numerical simulations with the volume-of-fluid method, Ohta *et al.* (2005) as well as Bonometti & Magnaudet (2006) indicated possibilities for obtaining spherical-cap bubbles at a few relatively large values of Reynolds number, such as $Re \sim 250$, 600, and 900, with properly arranged initial bubble deformations. Because of the transient nature of those volume-of-fluid simulations, whether those ‘large-Re’ spherical-cap bubbles correspond to steady-state solutions can only be answered tentatively (especially with the experimental evidence by Bhaga & Weber suggesting that spherical-cap bubbles of $Re > 110$ would develop unsteady wakes). Computing solutions directly based on steady-state governing equations, although not being able to reveal interesting dynamical processes, is an efficient way to study rigorously the steady states of a system (which deserve special attention in view of their theoretical and practical importance) and can also discover the unstable steady states with properly implemented solution branch tracking methods. To date, whether the experimentally observed spherical-cap bubble shape (especially that with steady, laminar wake) for $Re \geqslant 50$ corresponds to a solution branch of strictly steady axisymmetric Navier–Stokes equations for incompressible fluid flow remains open for further investigation.

The goal of the present work is to provide a definite answer to the existence of steady axisymmetric solutions for spherical-cap bubbles by computing solutions over large ranges of Reynolds number (i.e. $20 \leqslant Re \leqslant 500$) and Weber number (up to $We = 500$). A Galerkin finite-element method with full Newton iterations is used for simultaneously solving the steady axisymmetric Navier–Stokes equations for incompressible flow field together with the elliptic mesh generation equations for tracking the unknown bubble shape. Because the deformable bubble surface coincides with a finite-element mesh line, the computational method used here with a boundary-fitted mesh has been considered to offer the highest accuracy for the present type of problem (as noted by Tryggvason *et al.* 2001).

In what follows, the problem statement and solution method are presented in § 2, whilst computations of solutions of spherical-cap bubbles with specific continuation strategies are described in § 3. Steady-state solutions corresponding to bubbles with various shapes are explored in § 4 where the condition for solutions of bubbles with the spherical-cap shape is inferred, and the concluding remarks are provided in § 5 with suggestions for future investigations.

2. Problem statement and solution method

2.1. *Governing equations*

The problem considered here is a gas bubble of constant volume $(4\pi/3)R^3$ moving at a constant terminal velocity U along the centreline of a cylindrical container filled with a Newtonian liquid of density ρ and dynamic viscosity μ. The surface tension at the gas–liquid interface is denoted as γ and assumed to have a constant value. The viscous fluid flow is assumed to be incompressible, laminar, and axisymmetric. The radius of the cylindrical container R_c is set at one order of magnitude greater than R (i.e. $R_c = 10R$ as often used in experiments, e.g. Bhaga & Weber 1981), so the container wall is expected to have inconsequential effects on the bubble behaviour when the Reynolds number $Re \equiv 2\rho RU/\mu$ is no longer small (Van Dyke 1975), as in the cases studied here. In view of the fact that the density and viscosity of gases are typically orders of magnitude less than those of liquids, the hydrodynamic stresses due to the flow of gas inside the bubble is completely ignored in the present work.

The axisymmetric fluid flow of the liquid is governed by the steady incompressible Navier–Stokes equation system

$$\frac{1}{2} Re\, \boldsymbol{v} \cdot \nabla \boldsymbol{v} = \nabla \cdot \boldsymbol{T} \quad \text{with } \boldsymbol{T} \equiv -p\boldsymbol{I} + \nabla \boldsymbol{v} + (\nabla \boldsymbol{v})^T \tag{2.1}$$

and

$$\nabla \cdot \boldsymbol{v} = 0, \tag{2.2}$$

where the flow velocity vector $\boldsymbol{v}$ and pressure p are made dimensionless by measuring them in units of U and $\mu U/R$, respectively. Here R is used as the scaling length for non-dimensionalization, $\boldsymbol{I}$ denotes the identity tensor, and the superscript 'T' stands for the transpose.

For computational convenience, the mathematical problem is described in a reference frame moving with the bubble with the coordinate origin fixed at the centre of mass of the bubble. A cylindrical (z, r)-coordinate system is used with the z-axis coinciding with the axis of symmetry and pointing in the same direction as the far-field flow velocity. Thus, at the bubble surface, conservation of momentum is satisfied by imposing the traction boundary condition

$$\boldsymbol{n}\cdot\boldsymbol{T}=\frac{1}{Ca}\left[\frac{\mathrm{d}\boldsymbol{t}}{\mathrm{d}s}+\frac{\boldsymbol{n}}{r}\frac{\mathrm{d}z}{\mathrm{d}s}\right]+p_a\boldsymbol{n}-St\,z\boldsymbol{n}\quad\text{on } S_f, \tag{2.3}$$

where $Ca\equiv\mu U/\gamma$ is the capillary number, the local unit normal vector $\boldsymbol{n}$ at the free surface points from the liquid into gas, the local unit tangent vector $\boldsymbol{t}$ points in the direction of increasing s along the boundary and relates to $\boldsymbol{n}$ in such a way that $\boldsymbol{n}\times\boldsymbol{t}=\boldsymbol{e}_\theta$ (according to the right-handed coordinate system (z, r, θ)). The uniform excess pressure inside the bubble p_a is solved as an unknown to satisfy an overall constraint that the volume enclosed by the free surface S_f does not vary, namely,

$$\int_{S_f} r^2\frac{\mathrm{d}z}{\mathrm{d}s}\,\mathrm{d}s=\frac{4}{3}. \tag{2.4}$$

The Stokes number $St\equiv\rho\,g\,R^2/(\mu U)$ represents the buoyancy force and is also solved as an unknown to satisfy another overall constraint that the 'centre of mass' of bubble remains at the coordinate origin

$$\int_{S_f} z\,r^2\,\frac{\mathrm{d}z}{\mathrm{d}s}\,\mathrm{d}s=0. \tag{2.5}$$

As might be noted, the gravitational (body) force term does not explicitly appear in (2.1) because the hydrostatic pressure in the bulk liquid has been lumped in the generalized pressure p. Hence, the hydrostatic pressure effect due to buoyancy force only appears in the boundary condition (2.3) through St.

Moreover, the flow velocity field must satisfy

$$\boldsymbol{n}\cdot\boldsymbol{v}=0\quad\text{on } S_f \text{ and } r=0, \tag{2.6}$$

due to the kinematic condition at the free surface S_f, and the symmetry condition at the axis of symmetry $(r=0)$. In addition, the stress-free symmetric condition at the axis of symmetry $(r=0)$ can be expressed as

$$\boldsymbol{e}_z\boldsymbol{e}_r:\boldsymbol{T}=0\quad\text{at } r=0, \tag{2.7}$$

where $\boldsymbol{e}_z$ and $\boldsymbol{e}_r$ denote the unit vectors in the z- and r-directions, respectively. Because of the axisymmetry, any components of $\boldsymbol{T}$ associated with θ should vanish.

At the cylindrical container wall $(r=10)$ and the upstream (or 'inlet') boundary located at $z=-10$, the Dirichlet type of condition for far-field uniform flow velocity is imposed, i.e.

$$\boldsymbol{v}=\boldsymbol{e}_z\quad\text{on } r=10 \text{ and } z=-10. \tag{2.8}$$

At the downstream (or 'outflow') boundary $(z=20)$, the fully developed flow condition for hydrodynamic stresses is used, i.e.

$$\boldsymbol{e}_z\boldsymbol{e}_r:\boldsymbol{T}=\frac{\partial v_z}{\partial r}\quad\text{and}\quad\boldsymbol{e}_z\boldsymbol{e}_z:\boldsymbol{T}=-p_o\quad\text{on } z=20, \tag{2.9}$$

where the value of p_o is set to zero in the present work, as a natural choice.

2.2. Computational solution method

To compute numerical solutions of the present problem, the nonlinear system of partial differential equations (2.1)–(2.9) is discretized by Galerkin's method of weighted residuals with finite-element basis functions (see Strang & Fix 1973). In doing so, the problem domain (in zr space) is divided into a set of quadrilateral elements. On each element, which is mapped onto a unit square in the $\xi\eta$ (computational) domain, the unknown flow velocity is expressed in an expansion of biquadratic basis functions, while the pressure field is in an expansion of linear discontinuous basis functions to avoid over-constraint problems (Huyakorn *et al.* 1978). The finite-element mesh points around the deforming bubble surface are determined by a pair of elliptic partial differential equations (see Thompson, Warsi & Mastin 1985; Christodoulou & Scriven 1992; de Santos 1991)

$$\nabla \cdot (D_\xi \nabla \xi) = 0, \nabla \cdot (D_\eta \nabla \eta) = 0, \tag{2.10}$$

where the 'diffusion' coefficients D_ξ and D_η are locally adjustable parameters prescribed for generating a desirable distribution of mesh points in the problem domain. The mesh equations (2.10) can also be discretized by the Galerkin finite-element method. As described by Christodoulou & Scriven (1992), using the subparametric mapping for the mesh points can reduce the computational burden of solving the mesh equations (2.10) and is therefore adopted in the present work. Appropriate boundary conditions for (2.10) need to be specified to complete the mathematical description. For example, at the bubble surface, one of the boundary conditions for the mesh equations (2.10) is given by (2.6) along S_f and the other enforces the orthogonality of mesh lines to the free surface.

As a well-established approach,† the set of nonlinear algebraic equations of Galerkin's weighted residuals is simultaneously solved by Newton's method of iterations (Ortega & Rheinboldt 1970). At each Newton iteration, the Jacobian matrix of sensitivities of residuals to unknowns is evaluated with the values of unknowns determined in the previous iteration. The resulting linear algebra system is then solved by direct factorization of the Jacobian matrix with a modified version of Hood's frontal solver (Hood 1976). The iteration is continued until the L_2-norm of the residual vector becomes less than 10^{-8}. Newton's method usually renders quadratic convergence to the solution, if the initial estimate of the solution falls within the domain of convergence and the Jacobian matrix is implemented correctly.

The typical mesh used in the present problem is shown in figure 1, which contains 1712 elements and 7051 nodes, with 129 nodes along the bubble surface. Although coarser meshes used in previous studies of the similar problems (e.g. Ryskin & Leal 1984; Bozzi *et al.* 1997) were shown to be sufficient for most free-surface deformations, the present fine mesh is especially tested for adequately resolving large curvatures near the rim of spherical-cap bubbles. When computing more challenging cases such as those of spherical-cap bubbles at $Re \geqslant 200$, an even finer mesh with 161 nodes along the bubble surface is employed so as to avoid mesh-dependence problems.

It is known that the quality of finite-element computational results relies on the quality of the mesh. Noteworthy here is the importance of neglecting the fluid-dynamic

---

† The computational code used here was progressively developed by the author from an original version of Coating Flows Application Library in Professor L. E. Scriven's group at the University of Minnesota, which was used for (and attested with) various studies involving viscous fluid flows with free surfaces, such as Feng & Scriven (1992), Feng & Basaran (1994), Bozzi *et al.* (1997) and Feng (1998).

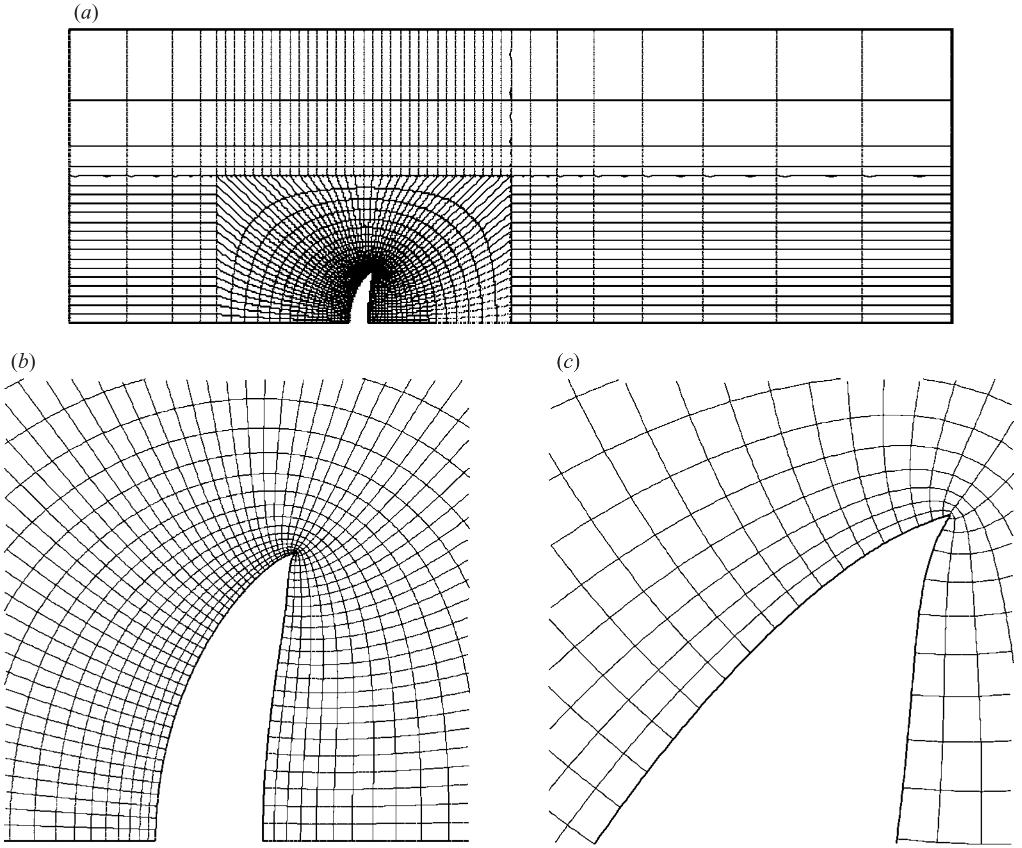

FIGURE 1. Finite-element mesh of the problem domain (as exemplified by the case of $Re = 100$ and $Ca = 2$): (a) entire problem domain; (b) detail around bubble; (c) detail around highly curved bubble rim.

effect of the gas phase inside the bubble. It enables computation of solutions with a highly distorted free surface to which the mesh lines can remain orthogonal (see figure 1). A high-quality quadrilateral mesh that can be retained even around the cusp-like point on a spherical-cap bubble rim would be very difficult to obtain if the flow field inside the bubble were also discretized and computed (e.g. Bozzi *et al.* 1997).

3. The solutions of spherical-cap bubbles

The successful solution of nonlinear equations by Newton iterations relies on sufficiently accurate initial estimates of the solution. If a solution for a given set of parameters is obtained, it can be used as the initial estimate for another nearby solution corresponding to one or more parameters being varied slightly in the parameter space. Thus, by varying the parameters in small steps from a 'first' solution, a family of solutions can be traced, in the sense of so-called zeroth-order continuation. Although more sophisticated continuation strategies (Riks 1972; Keller 1977) can be implemented for more efficient solution branch tracing, simple zeroth-order continuation can be quite adequate for computing the solutions of spherical-cap bubbles in this section.

As might be noted, Reynolds number Re and capillary number Ca are the only two independent parameters in the present problem free for specification. Therefore, continuation by either varying Re while holding Ca fixed, or varying Ca while holding Re fixed, becomes straightforward. Here, the choice of Re and Ca as primary parameters to vary comes mainly from the consideration of computational convenience in exploring the steady-state solution space, with St determined as part of the solution. Once Re, Ca, and St are given, all other relevant dimensionless parameters such as drag coefficient C_D, Froude number, Bond number, etc., associated with a solution can all be calculated in terms of them. For example, the Weber number $We \equiv 2\rho U^2/\gamma$ (used in Ryskin & Leal 1984) can be expressed as $Re\,Ca$. Because of the non-dimensional form of governing equations adopted in the present work, each solution corresponding to a set of specified Re and Ca can represent numerous seemingly different fluid systems and bubble sizes by virtue of dynamical similarity (as discussed by Batchelor 1967). For instance, the terminal velocity U and size R of a bubble represented by a computed solution can be determined as $U = \sqrt{Re/2}\,[g\,\gamma\,Ca/(\rho\,St)]^{1/4}$ and $R = \sqrt{\gamma\,Ca\,St/(\rho\,g)}$ with fluid viscosity satisfying $\mu = \gamma\,Ca\sqrt{2/Re}\,[\rho\,St/(g\,\gamma\,Ca)]^{1/4}$. Thus, a series of solutions at various values of Re and Ca can be used to describe bubble behaviour in a large range of experimental conditions.

A convenient first solution for the present problem is obtained by solving the equation system of diminishing nonlinearity, such as that for $Re = 0$ and $Ca = 0.01$ (as a case almost equivalent to Stokes flow past a spherical bubble). Because of the container wall located at $r = 10$, the computed St ($\equiv \rho g R^2/(\mu U)$) is 3.49219, which is very close to 3.48972 – the analytical result of Haberman & Sayre (1958) for a spherical bubble moving in a cylindrical tube of radius 10 times the bubble radius. Thus, the upstream and downstream boundaries in the present problem domain are believed to be far enough even for Stokes flow at $Re = 0$, which is expected to be most sensitive to the errors in far-field boundary conditions.

3.1. *Solutions of* $20 \leqslant Re \leqslant 500$ *at fixed* $Ca = 1$

As is well documented by Ryskin & Leal (1984) and repeated by Sugiyama, Takagi & Matsumoto (2001), the spherical-cap shape of a bubble is well developed at $Re = 20$ and $We \geqslant 15$. But for $Re \geqslant 50$, increasing We does not seem to lead to the solutions that correspond to the spherical-cap bubble (Ryskin & Leal 1984; Christov & Volkov 1985; Ohta *et al.* 2005). Therefore, the attention here is mainly focused on solutions of spherical-cap bubbles for $Re > 20$ starting from the solution of $Re = We = 20$.

Continuation from the solution of $Re = 0$ and $Ca = 0.01$ to that of $Re = 20$ and $Ca = 0.01$ is simply done by using the former as the initial estimate. The solution for $Re = 20$ and $Ca = 0.01$ is obtained with five Newton iterations. Because the bubble shape is essentially spherical (at $We = 0.2$ with an aspect ratio $\alpha \equiv 2r_{max}/(z_{max} - z_{min})$ of 1.0217, where r_{max}, z_{min} and z_{max} denote the maximum r-coordinate and minimum and maximum z-coordinate values of deformable bubble surface), the computed drag coefficient

$$C_D \equiv \frac{16St}{3Re} \tag{3.1}$$

for this case is 1.45235. Holding Re fixed at 20 and gradually increasing the value Ca to 0.75, a solution of $We = 15$ is obtained, as shown in figure 2(*a*), which appears to be in good agreement with the result of Ryskin & Leal (1984), who also showed a close comparison with the experimental photograph by Hnat & Buckmaster (1976) for $Re = 19.4$ and $We = 15.3$. For the convenience of comparison and future reference,

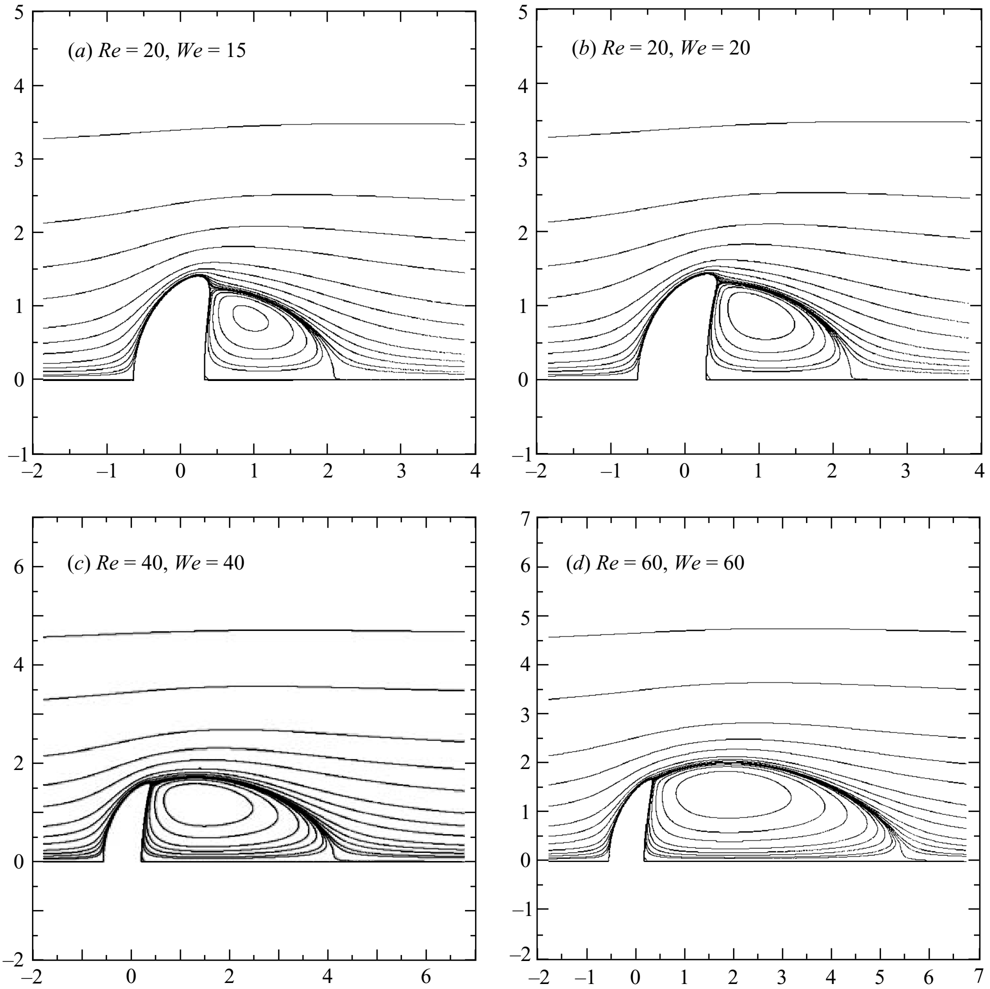

FIGURE 2. Streamlines and bubble shape for (a) $Re = 20$ and $Ca = 0.75$ ($We = 15$, $Mo = 0.0545$), (b) $Re = 20$ and $Ca = 1$ ($We = 20$, $Mo = 0.1312$), (c) $Re = 40$ and $Ca = 1$ ($We = 40$, $Mo = 0.0577$), (d) $Re = 60$ and $Ca = 1$ ($We = 60$, $Mo = 0.0355$).

the contour values for streamfunction shown in figures of the present work are 0, ± 0.001, ± 0.002, ± 0.005, ± 0.01, ± 0.02, ± 0.05, ± 0.1, etc., like those in Ryskin & Leal (1984). The drag coefficient computed here is $C_D = 3.4409$, whereas Ryskin & Leal (with a much coarser mesh) obtained 3.55 and Hnat & Buckmaster 3.44.

If Ca is further increased to 1 ($We = 20$) and 2 ($We = 40$), the computed drag coefficient, respectively, becomes $C_D = 3.49864$ and 3.54931, whereas the empirical formula of Bhaga & Weber (1981) for high Morton number ($Mo \equiv (3/4) C_D We^3/Re^4 = (3/4) C_D Ca^3/Re > 4 \times 10^{-3}$)

$$C_{D-emp} = \left[(2.67)^{0.9} + \left(\frac{16}{Re} \right)^{0.9} \right]^{1/0.9} \tag{3.2}$$

yields a value of 3.68994 for drag coefficient at $Re = 20$. As shown in figure 2(b), the bubble of $Re = 20$ and $We = 20$ has greater surface curvature at the rim with enlarged recirculation zone than that of $We = 15$ (see figure 2a). This observation agrees with the mechanism discussed by Ryskin & Leal (1984) that in the low-Re range, i.e. $Re \leqslant 20$, the bubble shape in an overall sense does not differ much with the variation of We for large We (at fixed Re). However, the surface curvature at the rim and the amount of vorticity in the wake may still increase with We.

With Ca held at a fixed value of 1, the solution of $Re = We = 40$ can be obtained using the solution of $Re = We = 20$ as the initial estimate for Newton iterations. As expected, the recirculation zone with the bubble of $Re = We = 40$ in figure 2(*c*) is greater than that of figure 2(*b*) for $Re = We = 20$. Further increasing Re to 60 at fixed $Ca = 1$ yields the solution shown in figure 2(*d*) (for $We = 60$). It is interesting to note that the spherical-cap bubble shape at $Re = We = 40$ and 60 is almost invariant, albeit with visually undetectable, highly localized differences. However, the size of the recirculation eddy in the wake increases with Re and We.

To evaluate mesh-sensitivity of the computed results, the value of drag coefficient C_D is examined with difference meshes. For the case of $Re = We = 100$, the value of C_D is computed as 2.53106 with the mesh (as in figure 1) having 129 nodes along the free surface. If meshes with 97 nodes and 161 nodes on the bubble surface were used, the results would be 2.53003 and 2.53017, respectively. Mesh-sensitivity is reduced with decreasing Re. For example, at $Re = We = 50$, the computed values of C_D become 2.94747, 2.94701, and 2.94653, with meshes having 97, 129, and 161 nodes on the bubble surface, respectively. At $Re = We = 200$, however, the computed C_D values become 2.15635, 2.12286, and 2.11817 with increasing number of nodes on bubble surface. If $Re = We$ is increased to 500, the computed C_D values are 1.92713, 1.82347, and 1.80338 when refining the mesh. Thus, using the finest mesh (with 161 nodes along bubble surface) for computing cases of $200 \leqslant Re \leqslant 500$ is expected to keep the variation of C_D less than 1%. For cases of $Re \leqslant 100$, the mesh shown in figure 1 can be quite adequate for accurate computations.

The present finite-element code can be used to compute cases of $20 \leqslant Re \leqslant 500$, at a fixed value of $Ca = 1$ without exhibiting any numerical difficulties. Figures 3(*a*)–3(*c*) show the streamlines and bubble shape for $Re = We = 100$, 300, and 500, respectively. The bubble of $Re = We = 100$ in figure 3(*a*) appears to retain the same spherical-cap shape as those in figures 2(*c*) and 2(*d*) for lower $Re = We$, except for the larger recirculation eddy in the wake. As the value of $Re = We$ is increased to 300 and 500 the size of the recirculation eddy is further enlarged, while the bubble still exhibits the same spherical-cap shape (see figure 3). With the value of $Re = We$ increased from 300 to 500, the streamwise length of the recirculation eddy does not seem to change, but width of the recirculation eddy still increases slightly.

The experimental data summarized by Bhaga & Weber (1981) show that the width of wake increases with Re up to $Re \sim 100$, with wake width measured in units of bubble diameter for a wide range of Mo values approximately equal to 1.2, 1.7, and 2.3 at $Re = 20$, 50, and 100, respectively. Evaluated from the computed results at $Re = 20$, 50, and 100, the corresponding values of the wake width (in units of bubble diameter) are found about 1.31, 1.88, and 2.50. The values of the wake length in units of bubble diameter shown by Bhaga & Weber are approximately 1.0, 2.0, and 3.0 for $Re = 20$, 50, and 100, respectively, whereas those from computed results indicate about 0.979, 2.33, and 3.33. Thus, the computed bubble wake structures seem to compare reasonably with the experimental data presented by Bhaga & Weber (1981).

The spherical-cap appearance of the bubble shape found in experiments led Davies & Taylor (1950) to measure the actual surface profile from the photographic images for comparison with a circular arc. They concluded that 'the upper part of the bubble is a portion of a sphere within the experimental error.' However, the analyses

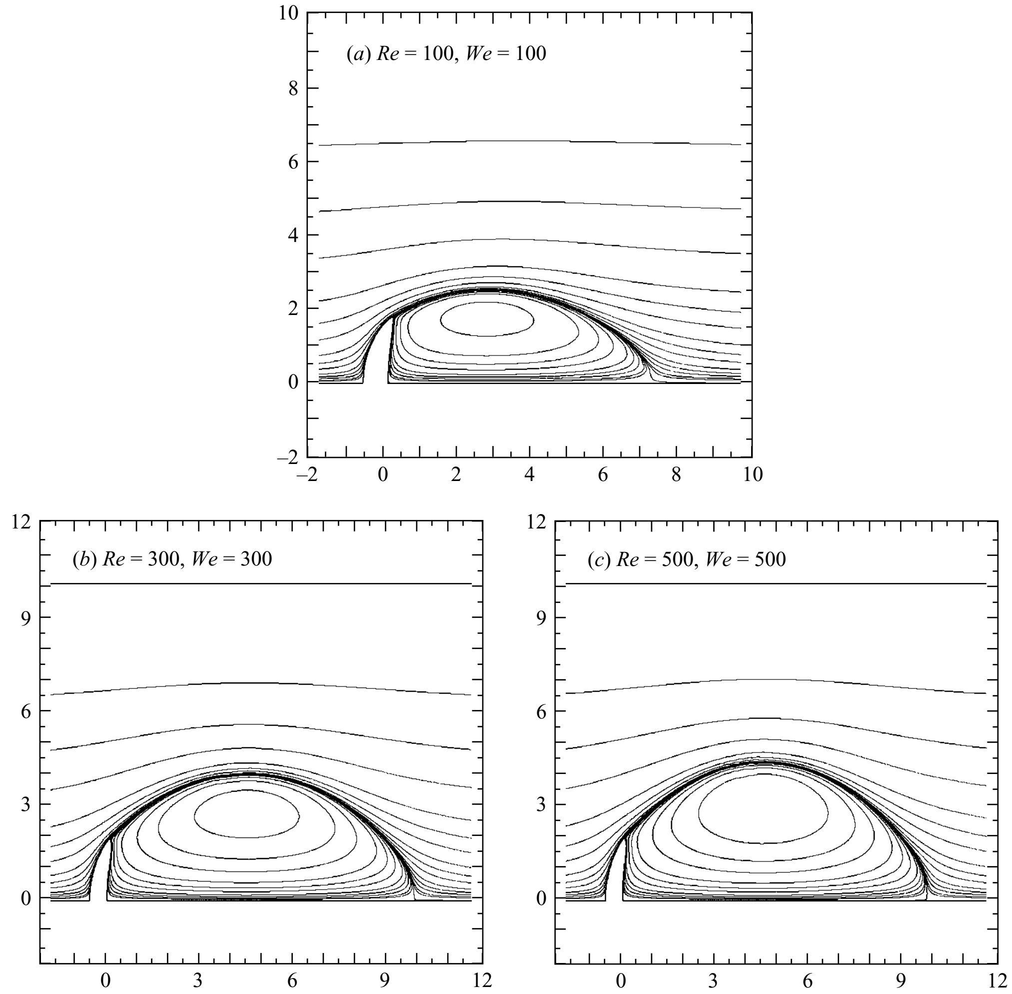

FIGURE 3. Streamlines and bubble shape for (*a*) $Re = 100$ and $Ca = 1$ ($We = 100$, $Mo = 0.0190$), (*b*) $Re = 300$ and $Ca = 1$ ($We = 300$, $Mo = 4.78 \times 10^{-3}$), (*c*) $Re = 500$ and $Ca = 1$ ($We = 500$, $Mo = 2.71 \times 10^{-3}$).

of Collins (1966) and Joseph (2003) suggest that the front portion of the bubble may not be an exact circular arc. If the front part (or upper part, as referred to by Davies & Taylor), of the bubble surface indeed fits a portion of a sphere, the radius of curvature of computed 'spherical-cap' bubble surface may be simply evaluated based on two bubble-surface nodal positions $(z_{stag}, 0)$ (where z_{stag} denotes the z-coordinate value of the front stagnation point) and (z_n, r_n) by

$$R_{cap} = \frac{(z_n - z_{stag})^2 + r_n^2}{2(z_n - z_{stag})}, \tag{3.3}$$

where (z_n, r_n) can be any nodal coordinates on the front part of the bubble surface other than $(z_{stag}, 0)$. Equation (3.3) is derived using the formula for a circle $(z - z_c)^2 + r^2 = R_{cap}^2$, with z_c and R_{cap} determined by two given points on the circle. Unfortunately, a simple test for the case of $Re = We = 100$ with several selected nodes on the front part of the bubble surface shows that the calculated R_{cap} with (3.3) varies from

Re	C_D	C_{D-emp}	Mo	r_{max}	z_{min}	z_{max}	R_{cap}	z_{wake}
20	3.49864	3.68994	0.1312	1.427	−0.634	0.429	1.624	2.242
30	3.24491	3.37466	0.0811	1.534	−0.593	0.411	1.797	3.271
40	3.07812	3.21250	0.0577	1.603	−0.568	0.395	1.935	4.128
50	2.94701	3.11306	0.0442	1.652	−0.551	0.378	2.048	4.856
60	2.83816	3.04558	0.0355	1.688	−0.537	0.362	2.144	5.484
80	2.66503	2.95947	0.0250	1.739	−0.516	0.335	2.313	6.507
100	2.53106	2.90658	0.0190	1.775	−0.500	0.315	2.457	7.295
200	2.11817	2.79653	7.94×10^{-3}	1.887	−0.450	0.276	3.010	9.383
300	1.91068	2.75778	4.78×10^{-3}	1.951	−0.422	0.264	3.404	9.852
400	1.82487	2.73773	3.42×10^{-3}	1.980	−0.409	0.255	3.612	9.787
500	1.80338	2.72540	2.71×10^{-3}	1.984	−0.405	0.247	3.667	9.783

TABLE 1. Values of C_D [compared with C_{D-emp} in (3.2)], $Mo=(3/4)C_D/Re$, r_{max}, z_{min}, z_{max}, R_{cap}, and z_{wake} for $20 \leqslant Re \leqslant 500$ at $Ca=1$ ($We=Re$).

2.3838 (with the node at the bubble rim) to 2.6853 (with the node next to the front stagnation point), indicating that the front part of the bubble surface is not exactly a portion of a sphere. Therefore, the value of R_{cap} in the present work is evaluated by fitting the bubble front part of nodal position values to a sphere with a least-squares method.† For example, the value of R_{cap} for $Re=We=100$ is obtained as 2.457 by the least-squares evaluation. The values of variance‡ are found to be typically less than 10^{-4} when evaluating R_{cap} for various Re and We, suggesting that the steady, axisymmetric solutions of bubbles presented here (for $We \geqslant Re$) indeed exhibit the profile with the front part quite close to a portion of a sphere.

Table 1 shows the computed values of C_D compared with the empirical formula of Bhaga & Weber (1981) given in (3.2); the radius of bubble cross-section r_{max} (i.e. $2r_{max}$ represents the maximum transverse, dimension); the minimum and maximum z-coordinate values on the bubble surface z_{min} and z_{max}, the radius of the spherical cap R_{cap}, and the z-value at the axis of symmetry z_{wake} with $v_z=0$ indicating the end of the recirculation zone in the wake, for $20 \leqslant Re \leqslant 500$ at fixed $Ca=1$.

Although the computations of steady, axisymmetric solutions can be extended up to $Re=500$ and greater at $Ca=1$, many experiments indicated that bubbles with closed, laminar toroidal wakes may only be observed for $Re<200$ (Wegener & Parlange 1973; Hnat & Buckmaster 1976). For example, the results of Wegener & Parlange (1973) suggest that instability may set in when $Re>180$, whereas Bhaga & Weber (1981) found the wake behind the bubble becomes open and unsteady for $Re>110$. Therefore, the computed solutions here for $Re>200$ are not expected to provide predictions of real-world observable phenomena, but rather to satisfy theoretical curiosities.

In general, the computed C_D seems to be lower than C_{D-emp}. This may be attributed to the fact that a small amount of surfactant or other impurities, which is usually difficult to eliminate in experiments, can increase the drag force on bubbles (as discussed by Levich 1962, Levich & Krylov 1969, and computationally shown by Sugiyama *et al.* 2001). But the trend of discrepancy increases with $Re=We$ is still somewhat puzzling. According to table 1, however, the agreement between C_D and

---

† By solving for R_{cap} and z_c to minimize $\sum[R_{cap}^2-(z_n-z_c)^2-r_n^2]^2$, where the summation includes all the nodes from the stagnation point to that corresponds to r_{max}.

‡ Defined as $\sum[R_{cap}-\sqrt{(z_n-z_c)^2+r_n^2}]^2/N$, where N is the number of participating nodes from that at the front stagnation point to the one corresponding to r_{max}.

C_{D-emp} actually appears reasonable for $Re \leqslant 100$ (with a difference of less than 15% at $Re = 100$). Hence, the significant difference between C_D and C_{D-emp} for $Re > 100$ may be explained by the unsteady wakes observed by Bhaga & Weber (1981) for $Re > 110$, which is expected to lead to a quite different hydrodynamic stress distribution around the bubble surface from that of the steady, axisymmetric solutions computed in the present work.

Based on the theory of viscous potential flow (v.p.f.), Joseph (2003) derived a drag law for large *Mo* with an elegant form:

$$C_{D-v.p.f.} = \frac{1}{R_{cap}}\left(6 + \frac{32}{Re\,R_{cap}}\right). \tag{3.4}$$

Without general information about R_{cap} for various values of *Re*, Joseph (2003) used the information of Davies & Taylor (1950) at the asymptotic large-*Re* limit to obtain

$$\tilde{C}_{D-v.p.f.} = 0.445\left(6 + \frac{32}{Re}\right), \tag{3.5}$$

which is found to predict slightly lower values but generally is in very good agreement with (3.2) for a large range of *Re* from 10^{-1} to 10^3. Substituting the computed values of R_{cap} at various *Re* from table 1 into (3.4) yields $C_{D-v.p.f.} = 4.301$, 3.082, 2.495, 2.011, and 1.641, respectively, at $Re = 20$, 50, 100, 200, and 500, whereas (3.5) yields $\tilde{C}_{D-v.p.f.} = 3.382$, 2.955, 2.812, 2.741, and 2.699. The agreement between the presently computed C_D (see table 1) and Joseph's (3.4) appears to be excellent for $Re > 40$ (up to 500), especially for $50 \leqslant Re \leqslant 200$. Unlike $C_{D-v.p.f.}$, however, $\tilde{C}_{D-v.p.f.}$ (given in (3.5)) compares better with presently computed C_D for smaller *Re*, with discrepancy increases at larger *Re* (similar to (3.2)).

It is interesting to note that the variation of C_D is drastically reduced for $Re \geqslant 100$. For example, for $100 \leqslant Re \leqslant 200$ the value of C_D varies no more than $\pm 10\%$. Wegener & Parlange (1973) summarized experimental results indicating that the Froude number $Fr \equiv 2\sqrt{2/(3C_D)}$ becomes almost a constant of a value about unity for $Re \geqslant 100$. Based on the computed C_D values in table 1 for $Re = 100$ and 200, the Froude number takes values of $Fr = 1.026$ and 1.122, respectively.

From the values of r_{max} and R_{cap} provided in table 1, the value of the so-called cap angle θ_m can be calculated by $\sin^{-1}(r_{max}/R_{cap})$. For example, the cap angle for $Re = We = 20$, 50, 100, and 200 are $\theta_m = 61.49^\circ$, 53.77°, 46.26°, and 38.82°, respectively. The trend of θ_m decreasing with *Re* and approaching an asymptotic value at large *Re* seems to agree with the experimental observations suggesting an asymptotic value of θ_m for $Re > 100$ between 40° and 55° (see Wegener & Parlange 1973).

In their attempt to gain a basic understanding of a spherical-cap bubble, Davies & Taylor (1950) derived a relation between the bubble terminal velocity and the radius of curvature of the frontal surface based on inviscid potential-flow approximation,

$$U^2 = \frac{4}{9} g R R_{cap}, \tag{3.6}$$

where R_{cap} is computed here as a dimensionless variable measured in units of *R*. In terms of the dimensionless parameters in the present work, (3.6) can be rewritten as

$$We = \tfrac{8}{9}\,St\,Ca\,R_{cap} = \tfrac{1}{6} C_D Re\,Ca\,R_{cap},$$

which leads to

$$C_D R_{cap} = 6. \tag{3.7}$$

Using the values of C_D and R_{cap} in table 1, the values of $C_D R_{cap}$ for $Re = We = 20$, 50, 100, and 200 are found as 5.682, 6.035, 6.219, and 6.376, respectively. The agreement of present results for spherical-cap bubbles with steady laminar wake with the prediction of Davies & Taylor (1950) is not unreasonable; and the general agreement can be further improved if the higher-order correction of Collins (1966), i.e. $C_D R_{cap} = 6.273$, is used, especially for $50 \leqslant Re \leqslant 200$. Yet the potential-flow approximation used by Davies & Taylor (1950) and Collins (1966) is supposed to be more applicable to the spherical-cap bubbles at much larger Re with turbulent wakes. According to Joseph's (2003) viscous potential flow formula (3.4), however, the value of $C_{D-v.p.f.} R_{cap}$ should be equal to $6 + 32/(Re\, R_{cap})$, which leads to 6.985, 6.313, 6.130, and 6.053, respectively, at $Re = 20$, 50, 100, and 200; only slightly differing from the corresponding $C_D R_{cap}$ values, except for smaller Re such as $Re = 20$, when the difference between C_D and $C_{D-v.p.f.}$ becomes rather significant. But with (3.5) the value of $\tilde{C}_{D-v.p.f.} R_{cap}$ should be simply given by $0.445\, R_{cap}(6 + 32/Re)$, which yields 5.492, 6.051, 6.910, and 8.251, respectively, at $Re = 20$, 50, 100, and 200. Good agreement between $\tilde{C}_{D-v.p.f.} R_{cap}$ and $C_D R_{cap}$ for $Re = 20$ and 50 is not surprising because the value of $\tilde{C}_{D-v.p.f.}$ compares better with C_D in that range of Re.

3.2. *Solutions of $Ca > 1$*

Here, the steady-state spherical-cap solutions of $We > Re$ for $Re \leqslant 200$ are computed by increasing Ca in small steps at a fixed value of Re from the solutions of $Ca = 1$ (i.e. cases of $We = Re$). Figure 4 shows a couple of solutions at $Re = 20$ for $We = 40$ ($Ca = 2$) and 60 ($Ca = 3$), which illustrates the local curvature increase at the rim of bubble with increasing We. In fact, the local curvature at the bubble rim becomes so large for the case of $We = 60$ (figures 4*c*, 4*d*) that the bubble rim appears to be cusp-like. Further increasing We after the apparent cusp formation at the bubble rim makes it difficult to compute a converged solution. Even sometimes converged solutions can be computed at much greater We (i.e. $Ca \gg 2$), the numerical accuracy of the result becomes questionable due to the concern of inadequately resolved local curvature with a conventional finite-element mesh. Therefore, no attempt is made here to compute solutions for Ca greater than that corresponding to apparent cusp formation at the bubble rim.

The trend of cusp formation at the bubble rim is further illustrated in figures 5 and 6 at $Re = 50$ and 200 for $Ca = 1$ and 2, where the cases of $Ca = 1$ show that the bubble rim has finite curvature and the cases of $Ca = 2$ show cusp formation. While the general bubble shape appears unchanged with increasing Ca (and We) at fixed Re, the cusp-like tip, locally at the bubble rim for increased Ca, bends downstream, suggesting a tendency to skirt formation. For a given Re, increasing Ca corresponds to increasing the ratio of viscous force to capillary force, to consistent with the discussion of Hnat & Buckmaster (1976) on skirt formation mechanisms. In fact, Hnat & Buckmaster (1976) determined the skirt formation criterion as $Ca \approx 2.3$ based on their experimental data for $Re > 50$, comparing well with the present computational finding that suggests skirt formation at $Ca > 2$ for $Re \geqslant 50$. In a 'shape regime' map for bubbles in liquids in terms of the Eotvos number Eo ($\equiv (3/4) C_D We$, also called the Bond number) and Re, Bhaga & Weber (1981) indicated skirt formation in parameter ranges of $10 \leqslant Re \leqslant 50$ and $Eo > 200$ (i.e. $Ca > 3.7$ for $Re \sim 20$ and $Ca > 1.8$ for $Re \sim 50$), which seems to be quite consistent with the present results.

For convenience of comparison, the computed values of C_D, Mo, r_{max}, etc., for a few selected cases of $We = 2Re$ are provided in table 2. The computed characteristic values in tables 1 and 2 indicate that the values of r_{max} and z_{max} increase with We

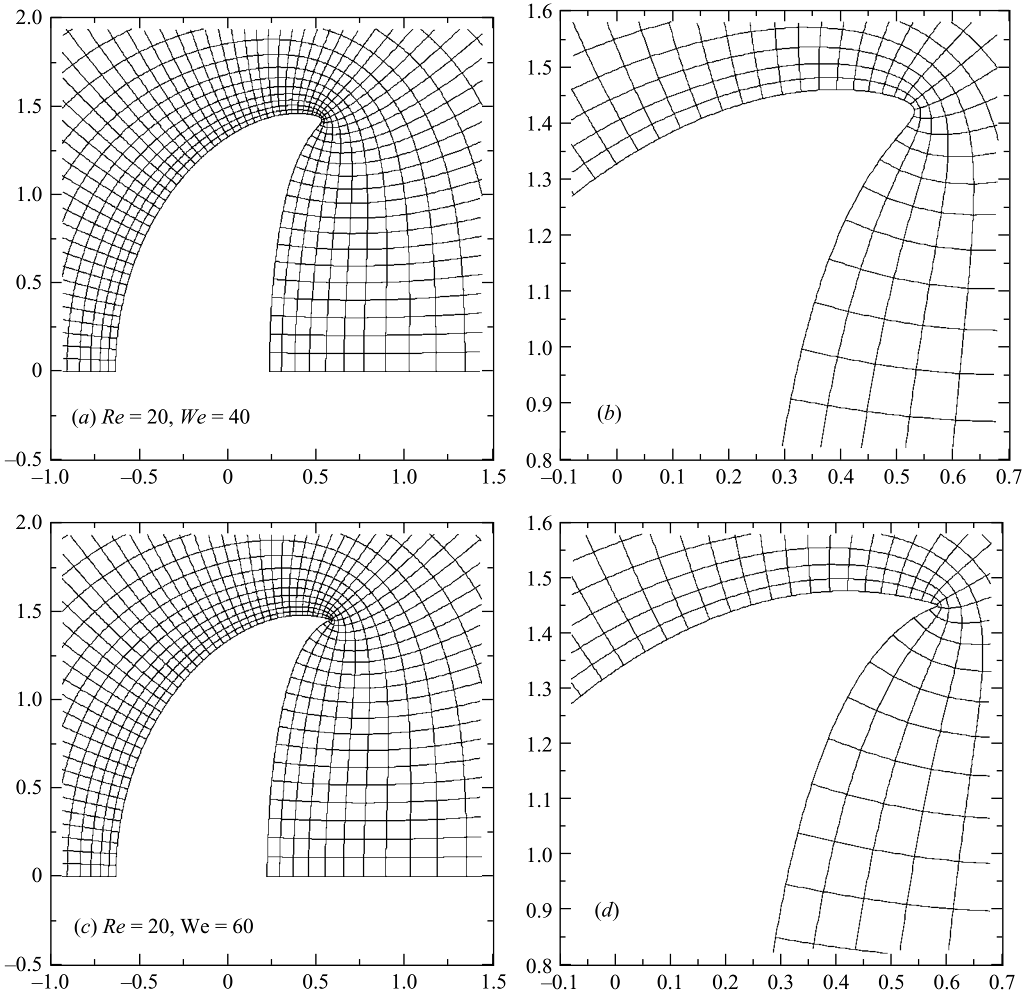

FIGURE 4. Mesh around bubble surface of $Re = 20$ with different magnifications for (*a*), (*b*) $Ca = 2$ ($We = 40$), and (*c*), (*d*) $Ca = 3$ ($We = 60$).

Re	C_D	Mo	r_{max}	z_{min}	z_{max}	R_{cap}	z_{wake}
20	3.54931	1.0647	1.459	–0.636	0.531	1.617	2.468
50	2.93170	0.3518	1.700	–0.550	0.450	2.021	4.923
100	2.51511	0.1509	1.819	–0.499	0.357	2.433	7.304
200	2.10969	0.0633	1.927	–0.449	0.284	2.978	9.374

TABLE 2. Values of C_D, $Mo = 6\,C_D/Re$, r_{max}, z_{min}, z_{max}, R_{cap}, and z_{wake} for $Ca = 2$ ($We = 2\,Re$).

corresponding to the cusp formation at bubble rim, whereas z_{min} remains unchanged corresponding to invariant general bubble shape and the centre of bubble volume. The slightly reduced cap radius R_{cap} appears to relate to a slightly reduced value of C_D for $Re \geqslant 50$ with unchanged wake size reflected in z_{wake}. A slight increase in C_D for $Re = 20$ from $Ca = 1$ to 2 seems to correspond to the slight increase of the value of z_{wake}. But the value of z_{wake} remains almost unchanged for $Re \geqslant 50$ with increasing

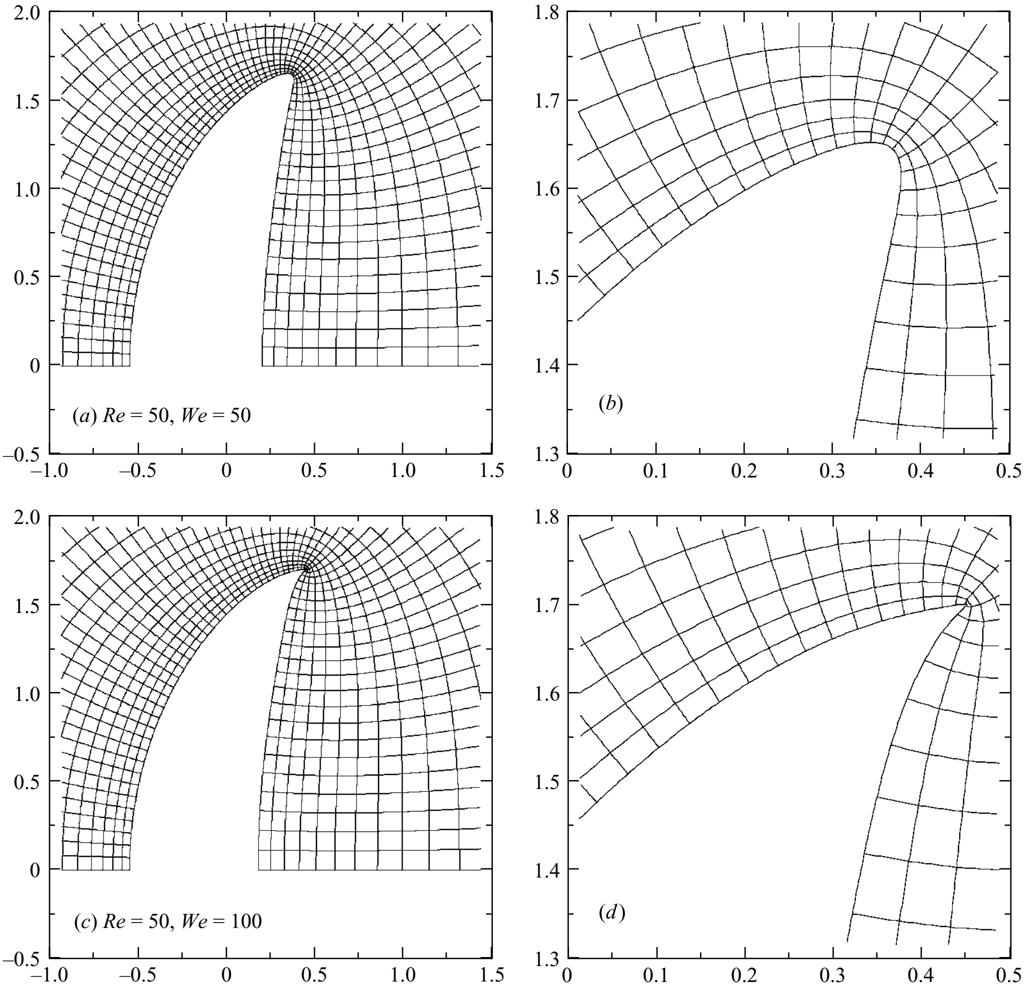

FIGURE 5. Mesh around bubble surface of $Re = 50$ with different magnifications for (*a*), (*b*) $Ca = 1$ ($We = 50$), and (*c*), (*d*) $Ca = 2$ ($We = 100$).

Ca from 1 to 2. For $Re = 20$ and $Ca = 3$ ($We = 60$), the values of C_D, r_{max}, z_{min}, z_{max}, R_{cap}, and z_{wake} are 3.54861, 1.476, –0.633, 0.584, 1.631, and 2.543, respectively. In general, the characteristic values in tables 1 and 2 as well as those for $Re = 20$ and $Ca = 3$ differ only by a few per cent, even with a substantial change in Ca (and We). Hence the experimentally observed spherical-cap bubbles are expected to exhibit behaviour basically independent of the value of Ca (or We) for $Ca \geqslant 1$ (or $We \geqslant Re$, consistent with the conclusion of Bhaga & Weber (1981) that, for $Mo > 4 \times 10^{-3}$, bubble behaviour only depends on Re), except for the localized surface curvature increase at bubble rim and skirt formation at higher Ca.

4. Solutions of bubbles with various steady, axisymmetric shapes

Moving in a viscous liquid, a bubble may exhibit a variety of steady shapes depending upon the values of Re and Ca (or We). For example, steady-state solutions have been computed for spherical-cap bubbles in § 3 for relatively large

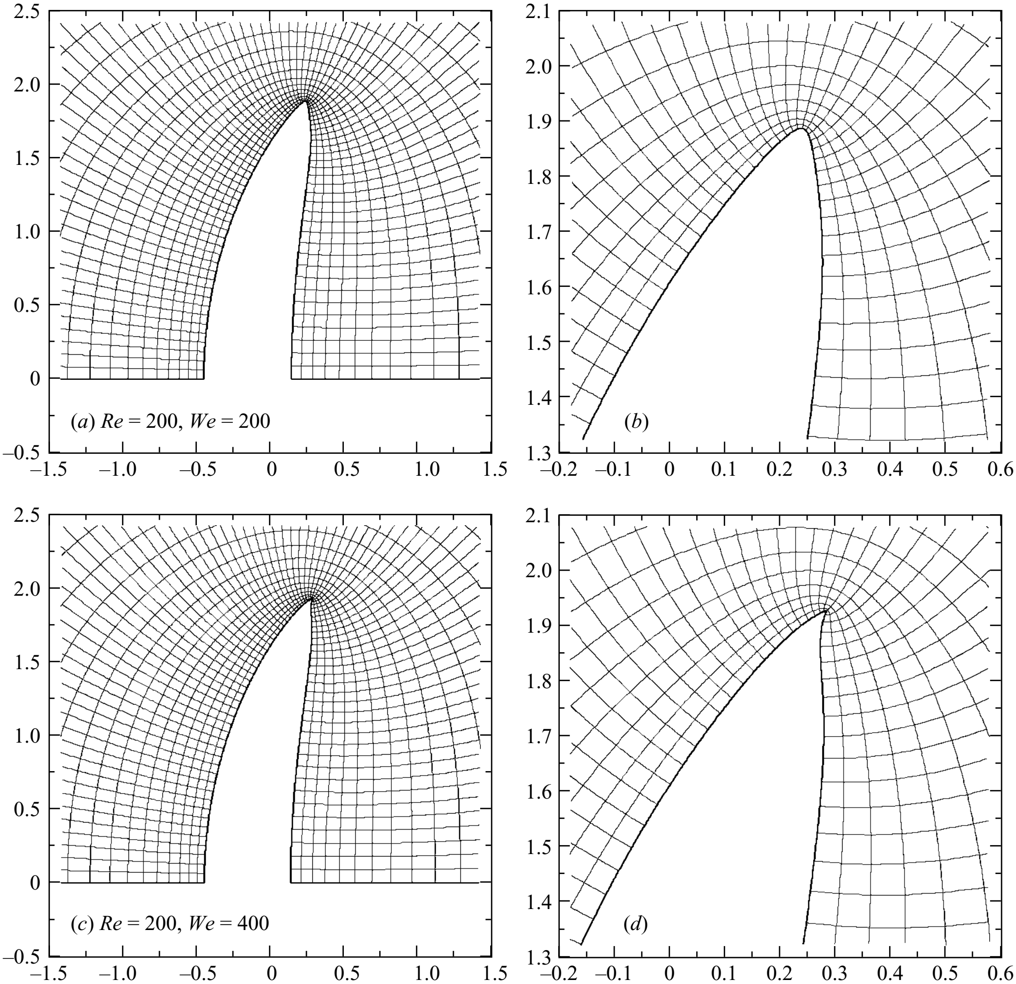

FIGURE 6. Mesh around bubble surface of $Re = 200$ with different magnifications for (a), (b) $Ca = 1$ ($We = 200$), and (c), (d) $Ca = 2$ ($We = 400$).

Ca (or $We \geqslant Re$), as often observed in the experiments (e.g. Davies & Taylor 1950; Haberman & Morton 1953; Wegener & Parlange 1973; Bhaga & Weber 1981) The disk-like and saucer-like bubbles were computed by many previous authors (cf. Ryskin & Leal 1984; Christov & Volkov 1985; Sugiyama *et al.* 2001; Ohta *et al.* 2005), usually at $Ca \ll 1$ or $We \ll Re$. Ryskin & Leal (1984) suggested the possibility of non-existence of steady axisymmetric bubbles above some critical values of We (for $Re \geqslant 50$).

Now, let us focus attention on the steady-state solutions of $We < Re$ computed by reducing Ca in small steps at a fixed value of Re from the solutions of $Ca = 1$ (i.e. cases of $We = Re$ in § 3.1). Up to $Re = 40$, the bubble shape changes gradually from that of a spherical cap to that of a sphere as $Ca \rightarrow 0$ from 1. But at $Re = 50$, reducing Ca from 1 corresponds to a decrease of local curvature around the bubble rim at first (see figure 7*a* for $Ca = 0.5$), as intuitively expected. The bubble shape becomes more fore–aft symmetric with continuously decreasing Ca, similar to that found by Ryskin & Leal (1984) for $Re = 50$ and $We = 10$. As Ca approaches 0.280

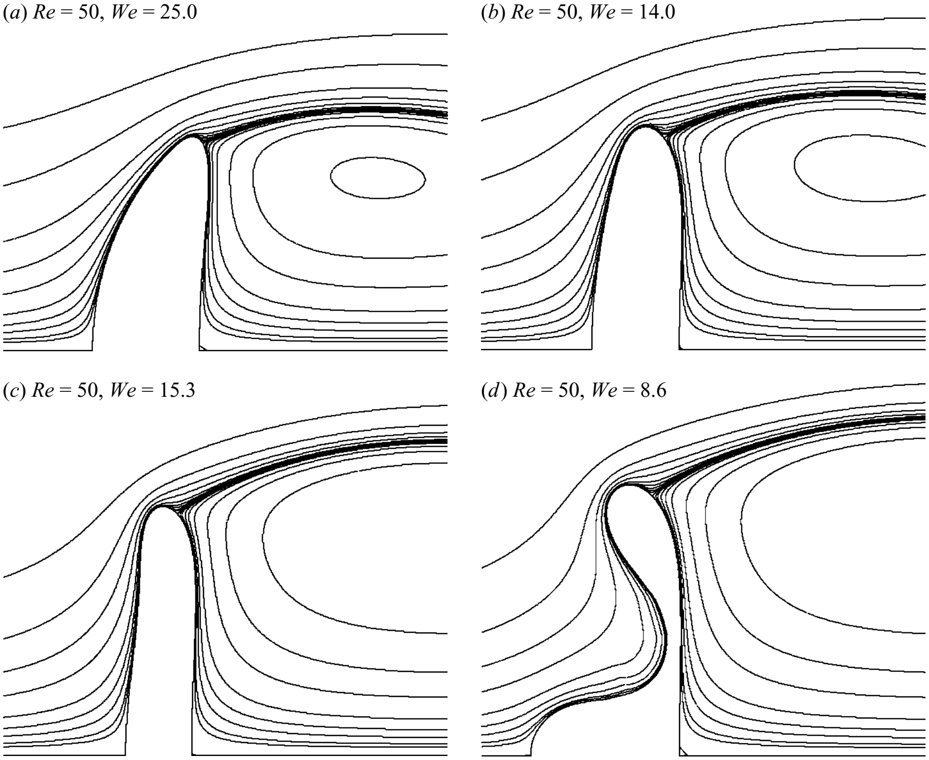

FIGURE 7. Bubble shapes and streamlines of solutions along the branch that connects the spherical-cap bubble at $Re = 50$ for (*a*) $Ca = 0.500$ ($We = 25$); (*b*) $Ca = 0.280$ ($We = 14$); (*c*) $Ca = 0.306$ ($We = 15.3$); (*d*) $Ca = 0.172$ ($We = 8.6$).

($We \sim 14.0$, figure 7*b*), however, a turning point is encountered where the Jacobian matrix for the Newton iterations becomes singular, with rank deficiency of one. The simple zeroth-order (or even more efficient first-order) continuation cannot be used to compute solutions along the solution branch beyond the turning point. Further continuation along the solution branch around turning points is enabled here by employing an arclength continuation algorithm, based on that of Keller (1977).† The solution branch folds back to increased value of Ca after this turning point, with more enhanced 'disk-like' bubble deformation until another turning point is encountered near $Ca \sim 0.306$ ($We \sim 15.3$, figure 7*c*), where the solution branch folds towards decreased Ca again. But further continuation along this solution branch no longer renders fore–aft-symmetric, disk-like bubble shapes; instead, the bubble appears more like a sombrero at smaller Ca (e.g. figure 7*d* for $Ca = 0.172$). Yet another turning point appears at $Ca = 0.172$ ($We = 8.60$), where the solution branch folds back to increased Ca. Stepping forward (with increasing Ca) leads to sombrero-shaped bubbles with such distorted meshes that the accuracy of the numerical solution becomes questionable. Therefore, the computations are not carried out much beyond the turning point at $Ca = 0.172$ in the parameter space.

On the other hand, the solution branches computed by increasing Ca in small steps, at a fixed value of $Re \geqslant 50$, from spherical bubble solutions at very small Ca, encounter

---

† Also exemplified by Boudouvis (1987) and Feng (2000).

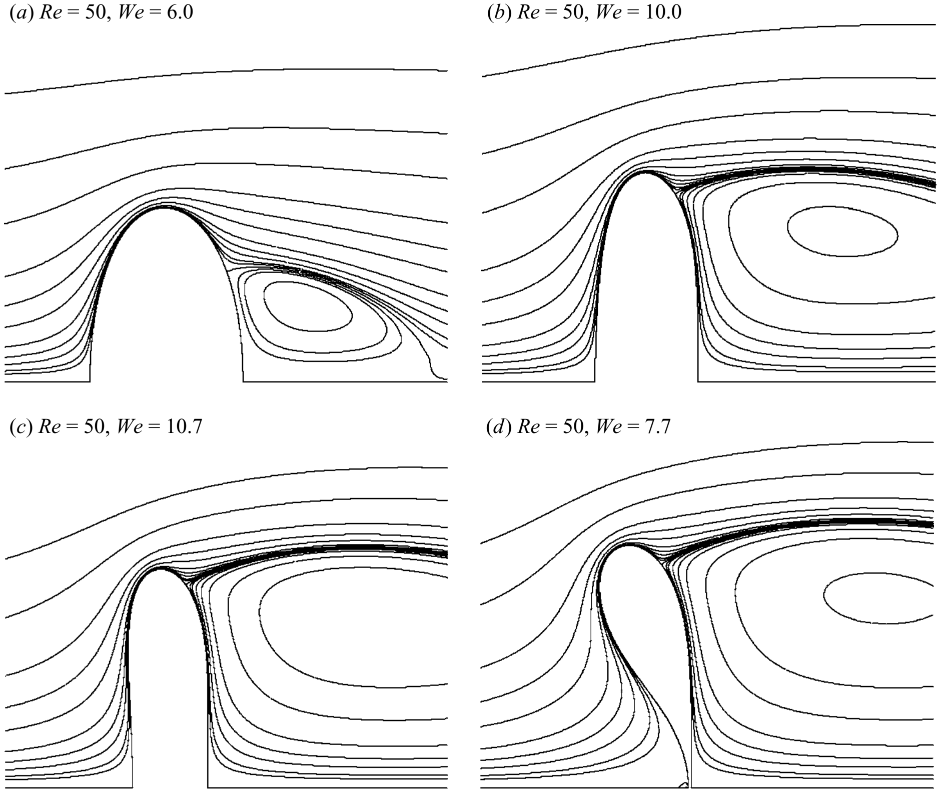
(*a*) $Re = 50$, $We = 6.0$
(*b*) $Re = 50$, $We = 10.0$
(*c*) $Re = 50$, $We = 10.7$
(*d*) $Re = 50$, $We = 7.7$

FIGURE 8. Bubble shapes and streamlines of solutions along the branch that connects to the spherical bubble at $Re = 50$ for (*a*) $Ca = 8.333$ ($We = 6$); (*b*) $Ca = 5.000$ ($We = 10$); (*c*) $Ca = 4.673$ ($We = 10.7$); (*d*) $Ca = 6.494$ ($We = 7.7$).

turning points at Ca slightly over 0.20, 0.10, and 0.05 (corresponding to $We = 10$) for $Re = 50$, 100, and 200, respectively. For example, at $Re = 50$ flow separation clearly occurs when $Ca = 0.12$ ($We = 6$) (figure 8*a*), as Ryskin & Leal (1984) had shown. At $Ca = 0.20$ the bubble takes a nearly fore–aft-symmetric disk-like shape (figure 8*b*), also comparable to the result of Ryskin & Leal (1984) at $We = 10$. With the present arclength continuation scheme, solutions beyond the turning point at $Ca = 0.2159$ ($We = 10.7964$) can be computed, although they are expected to be unstable with respect to even axisymmetric disturbances. More flattened bubble shapes and streamlines at $Ca = 0.214$ ($We = 10.7$ after the solution branch folds back beyond the turning point towards lower We) are shown in figure 8(*c*). Further continuation leads to the formation of doughnut-like bubble shapes with a hole developing at the thinning centre (figure 8*d* for $Ca = 0.154$ ($We = 7.7$)). Although converged solutions can still be computed with further continuation, those solutions correspond to unrealistic bubbles with the front stagnation point penetrating over the rear surface of the bubble.

The solution branches for $Re = 50$ are plotted in figure 9 in the parameter space of C_D versus We, where the turning points are illustrated and parameter points for solutions shown in figures 7 and 8 are indicated. For a given set of parameters, e.g. Re and Ca (or We), multiple solutions may exist for steady, axisymmetric bubbles corresponding to different values of drag coefficient C_D. However, whether any of

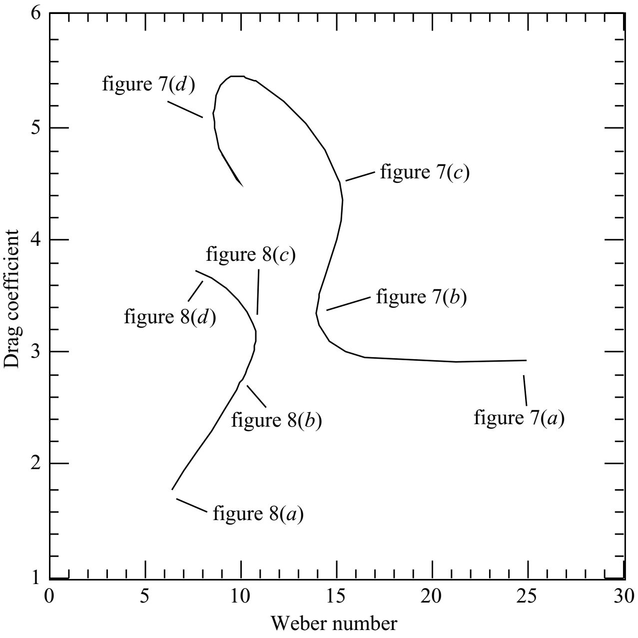

FIGURE 9. Solution branches in parameter space of C_D versus We for $Re = 50$.

those predicted solutions of steady, axisymmetric bubbles can be observed in the real-world experiments depends on their stability with respect to various types of disturbances. General stability analysis requires consideration of three-dimensional disturbances, which is beyond the scope of the present work.

The turning point on the branch extended from the spherical bubble, in the region of relatively small *We*, indicates local non-existence of steady axisymmetric bubbles above the critical value of *We* ($= 10.7964$ for $Re = 50$), as Ryskin & Leal (1984) speculated. The part of the branch beyond the turning point, folding back to lower *We*, is expected to represent unstable steady-state solutions (cf. Iooss & Joseph 1990). One of the interesting features described by this unstable part of the solution branch is that bubble deformation increases with decreasing *We*, somewhat contrary to physical intuition. Unstable solutions cannot be observed in real-world experiments. It should be noted that local non-existence of steady axisymmetric bubbles above the critical value of *We* does not mean global non-existence of steady axisymmetric bubbles. It only suggests that any steady axisymmetric bubble that can be found above the critical value of *We* would exhibit some discontinuities in the parameter space, and therefore may not be obtained by the arclength continuation scheme with small steps of parameter variations from the turning point. In fact, the global existence of multiple steady states, and the existence of steady axisymmetric bubbles beyond the critical value of *We* (with a jump, or discontinuity, of C_D), can be observed in figure 9.

Some part of the branch extended from the spherical-cap bubble in the region of relatively large *We* represents intuitively expected bubble behaviour, as the bubble surface becomes less curved with decreasing *We*. But the part towards the low-*We* end of this branch seems to describe bubbles with a more complicated sombrero shape at smaller *We*, which has never been observed in experiments and therefore could represent unstable solutions. Further, At $Re \sim 50$, disk-like bubbles are shown to appear around $We \sim 15$ on the branch connecting to the spherical-cap bubble (as

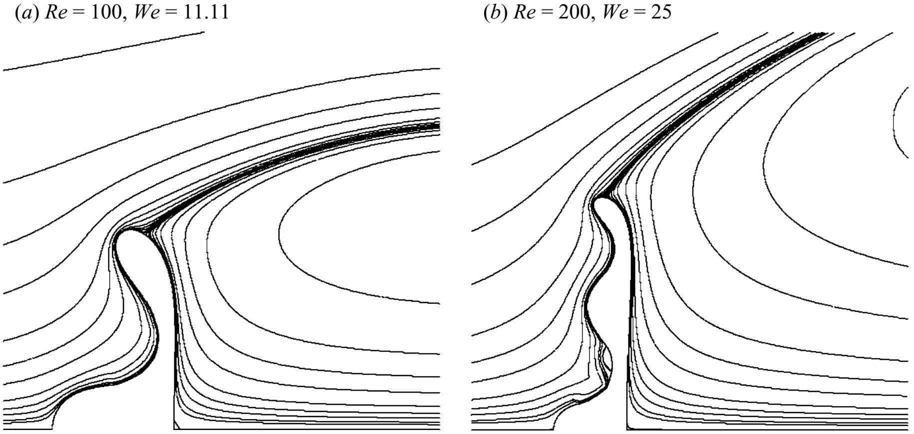

FIGURE 10. Bubble shapes and streamlines of (a) $Re = 100$ and $Ca = 0.1111$ ($We = 11.11$); (b) $Re = 200$ and $Ca = 0.1250$ ($We = 25$).

in figures 7*b* and 7*c*), besides that around the turning point on the branch in the relatively small We region (as in figures 8*b* and 8*c*). Indeed, the disk-like bubble observed by Bhaga & Weber (1981) for $Re = 55.3$ and $We = 15.4$ (in their figure 2*c*) was reported to wobble as it rose, indicating the instability of strictly axisymmetric bubbles.

For $Re = 100$, the solution branches in the parameter space of C_D versus We appear to be similar to that for $Re = 50$. Now the turning point on the branch extended from the spherical bubble in the small We region occurs at $We = 10.0306$, where the bubble takes the saucer-like shape. Further continuation along this branch after it folds back to lower We leads to the formation of doughnut-like bubbles (as in figure 8*d*). The solution branch traced by reducing Ca from the spherical-cap bubble (e.g. at $Ca = 1$) eventually leads to the sombrero-shaped bubble, as shown in figure 10(*a*). However, for $Re = 200$, reducing Ca from the spherical-cap bubble solution leads to a bubble shape with more bumps on the front (as in figure 10*b*), instead of the sombrero shape. But some of those complicated steady bubble shapes may serve to entertain theoretical curiosity, until confirmed by carefully arranged experiments. Thoroughly investigating the relationship and connectivities among those solutions associated with the complicated bubble shapes seen in figure 10 can be a very tedious task, often requiring frequent adjustment of mesh distributions for individual solutions to ensure numerical accuracy and reliability. It is therefore not pursued in the present work because the primary focus here is to search for conditions for steady, axisymmetric solutions of spherical-cap bubbles at $Re \geqslant 50$, as observed in real-world experiments.

Most of the variations in bubble shape seem to occur in the region of $Ca \ll 1$, as found by continuation with reducing Ca from the spherical-cap bubble at a given $Re \geqslant 50$. However, when the value of Ca is reduced to 0.5, bubbles appear still to retain the spherical-cap shape, although the curvature at the bubble rim decreases significantly (e.g. figure 7*a*). To provide a quantitative sense of change in spherical-cap bubble behaviour, a set of characteristic values for $Ca = 0.5$ such as C_D, R_{cap}, etc., are listed in table 3 for comparison with those at the corresponding Re for $Ca = 1$ and 2 in tables 1 and 2. The corresponding values in table 3 do not seem to vary from those in table 1 by more than 10%, especially for $Re \geqslant 50$. The most noticeable change is that the value of z_{wake} at $Re = 20$, indicating a reduced recirculating eddy, correlates

Re	C_D	Mo	r_{max}	z_{min}	z_{max}	R_{cap}	z_{wake}
20	3.24869	0.0152	1.368	−0.621	0.412	1.696	1.729
50	2.92719	5.49×10^{-3}	1.596	−0.542	0.323	2.156	4.684
100	2.53297	2.37×10^{-3}	1.712	−0.495	0.297	2.551	7.226
200	2.12460	9.96×10^{-4}	1.819	−0.447	0.276	3.105	9.335

TABLE 3. Values of C_D, $Mo=(3/32)C_D/Re$, r_{max}, z_{min}, z_{max}, R_{cap}, and z_{wake} for $Ca=0.5$ ($We=Re/2$).

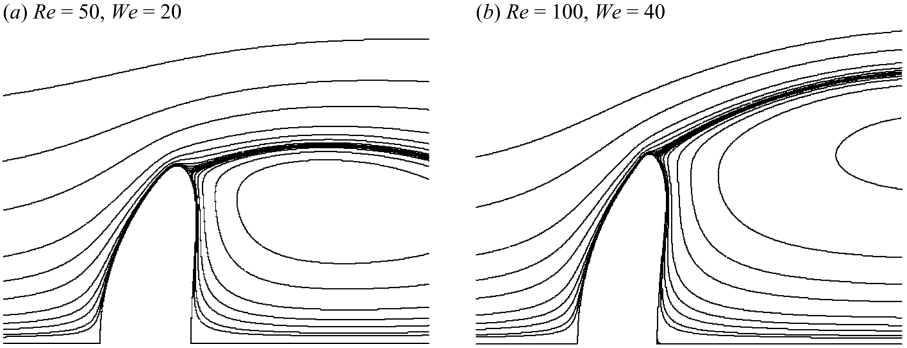

FIGURE 11. Bubble shapes and streamlines of (a) $Re=50$ and $Ca=0.4$ ($We=20$); (b) $Re=100$ and $Ca=0.4$ ($We=40$).

with the reduced local surface curvature at the bubble rim (Batchelor 1967; Ryskin & Leal 1984). However, the size of the recirculating eddy for $Re \geqslant 50$, at $Ca=0.5$, does not vary substantially, suggesting that at larger Re the convection effect could be the dominant factor in determination of the recirculating eddy size. Even when Ca is reduced to 0.4, the spherical-cap bubble shape may still be recognized, as shown in figure 11 for $Re=50$ and 100. For $Re=50$ and $Ca=0.4$ ($We=20$), the values of C_D, r_{max}, z_{min}, z_{max}, R_{cap}, and z_{wake} are 2.91665, 1.580, −0.536, 0.322, 2.251, and 4.602, respectively. For $Re=100$ and $Ca=0.4$ ($We=40$), the values of C_D, r_{max}, z_{min}, z_{max}, R_{cap}, and z_{wake} are 3.52824, 1.690, −0.492, 0.298, 2.621, and 7.186, respectively. It is noteworthy that the least-squares fitted R_{cap} here is quite accurate, with a variance typically on the order of 10^{-5}, indicating the front part of the bubble at $Ca=0.4$ is still very close to ‘a slice of a sphere’. But the rear part of the bubble appears to start bulging from the rim due to increased surface tension effects and thereby loses the flatness, as seen in classical spherical-cap bubble images. Thus, a conclusion may be drawn that steady axisymmetric solutions of spherical-cap bubbles can exist for $Ca > 0.4$, although the exact border line is difficult to define because the spherical-cap shape is lost gradually with decreasing Ca. The basic characteristics of spherical-cap bubbles (of $Ca \geqslant 0.5$ for a given $Re \geqslant 50$) are found almost independent of the value of Ca (or We), as shown in tables 1–3.

5. Concluding remarks

The existence of steady, axisymmetric solutions for spherical-cap bubbles, especially for $Re \geqslant 50$, is confirmed theoretically by using the Galerkin finite-element method for solving the nonlinear, free-boundary problem. Continuation by increasing Re at a fixed Ca (e.g. $Ca=1$) appears to be quite effective for computing spherical-cap bubbles.[†] The apparent cusp-like surface at the bubble rim, seemingly corresponding to skirt formation, for various $Re \geqslant 50$, is shown to occur around $Ca = 2$. This finding compares very well with the skirt formation criterion of $Ca \approx 2.3$ reported by Hnat & Buckmaster (1976), based on their experimental data for $Re > 50$. By exploring the parameter space, a sufficient condition for steady axisymmetric solutions of bubbles with the spherical-cap shape is found to be $Ca > 0.4$, with some level of arbitrariness in the definition of spherical-cap shape.

In computing the initial condition effect of bubble shape evolution, both Ohta *et al.* (2005) and Bonometti & Magnaudet (2006) showed possibilities of obtaining spherical-cap bubble at $Re \sim 250$, 600, and 900 all with $Ca < 0.4$, seemingly to disprove the condition of $Ca > 0.4$ for spherical-cap bubbles suggested by the present work. However, many experiments indicated that truly steady spherical-cap bubbles may only be realizable for $Re < 200$, beyond which the wake becomes unsteady (cf. Wegener & Parlange 1973, Hnat & Buckmaster 1976, Bhaga & Weber 1981, who even found that the wake becomes unsteady for $Re > 110$). Therefore, the exploration of parameter space carried out here is confined to $Re \leqslant 200$. Moreover, the condition suggested here for the steady spherical-cap bubble can only be regarded as a sufficient (but not necessary) condition, namely, with no indication that bubbles of $Ca < 0.4$ cannot have a spherical-cap shape. Owing to the non-uniqueness of steady-state solutions to the nonlinear equation system, conclusions can only be drawn based on what has been found.

It is noteworthy that the spherical-cap bubble shape remains almost unchanged for different Re ($\geqslant$50) at a given value of Ca ($\geqslant$0.5). In a large range of Re the behaviour of spherical-cap bubbles seems to be mostly determined by Ca instead of We, indicating the importance of local viscous effects even at $Re \sim 100$. The boundary-integral computations of Miksis, Vanden-Broeck & Keller (1981) for pure potential flow past a deformable bubble could only predict fore–aft-symmetric bubble shapes without flow separation in the wake. When viscous effects were approximately included in the boundary-integral computations (yet still with flow separation ignored), the bubble shape with rounded front surface and flat rear surface could be obtained by increasing Mo (Miksis, Vanden-Broeck & Keller 1982), again suggesting the important role of viscosity played in spherical-cap shape formation. Further evidence of non-negligible viscous effects on spherical-cap bubbles is that flow separation at the bubble rim is shown in the present computational results to always accompany a spherical-cap bubble, as is experimental results in the literature.

Continuation at a fixed $Re \geqslant 50$ by increasing Ca (or We) from an infinitesimal value, when the bubble takes a nearly spherical shape, cannot lead to the solutions of spherical-cap bubbles, but rather to the turning points where the solution branch folds back to reduced values of Ca (or We) corresponding to formation of doughnut-shaped bubbles. These turning points at various Re seem to be primarily determined by the value of We instead of Ca, because they all occur at We slightly above 10 (similar to the findings of Feng & Basaran 1994 for supported two-dimensional bubbles). Thus, the viscous effect on bubble shapes in the small We regime are not expected to be

---

[†] Without carrying out the actual computations, Ryskin & Leal (1984) speculated the possibility of reaching spherical-cap bubble solutions of $Re \geqslant 50$ by increasing Re while holding We constant, from the solution of spherical-cap bubble at $Re = We = O(20)$. Based on the findings of the present work, this approach may indeed be viable. However, the bubbles for $Re > 50$ at $We = 20$ may not exhibit the classical spherical-cap shape. But they may lead to solutions of classical spherical-cap bubbles by increasing We.

important, in contrast to that on spherical-cap bubbles. This fundamental difference may provide a phenomenological reason for the disconnectivity of solution branches extended from solutions of spherical bubble and that from spherical-cap bubble solutions for $Re \geqslant 50$.

But continuation at a fixed $Re \geqslant 50$ by reducing Ca (or We) from that for spherical-cap bubbles, e.g. $Ca = 1$, tends to end up with complicated bubble shapes such as sombreros, or with even more bumps on the front surface (cf. figure 10). The solution branches extended from spherical-cap bubbles at relatively large Ca ($\sim$1) do not seem to connect to the spherical bubbles at small Ca (or We) for a fixed value of Re. Even though multiple steady, axisymmetric solutions are shown to exist for a given set of parameters, their stability with respect to arbitrary, three-dimensional disturbances is not analysed within the present mathematical framework. Only stable solutions are expected to be observed in laboratory experiments. Yet our intuitions are mostly formed based on phenomena observed in the real world: hence, the counter-intuitive trend that some of those steady, axisymmetric bubble shapes, with complicated features becoming more pronounced with decreasing Ca, are likely to be unstable.

Although the existence of steady axisymmetric solutions for spherical-cap bubbles at $Re \geqslant 50$ is determined herewith (as a primary goal), the complicated solution branch connectivities and a variety of steady axisymmetric bubble shapes, revealed as a by-product of the present work in exploring the parameter space, suggest ample interesting subjects for future investigations. To compute conveniently the solutions for bubbles with complicated shapes, a more versatile mesh generation scheme is desired, with somewhat automated adaptivities (e.g. as presented by Chen, Schunk & Sackinger 1995 and Sackinger, Schunk & Rao 1996). A thorough analysis of the solution connectivities and fold tracking in parameter space can be facilitated by using the algorithms extensively described by Musson (2001) following the works of Keller (1977), Stewart (1981), Chan (1984), etc. Then, the linear stability of the steady axisymmetric solutions with respect to three-dimensional disturbances can be analysed by solving the generalized eigenproblem as exemplified by Christodoulou (1989) and Carvalho (1996). A stable steady axisymmetric solution should be observable in laboratory experiments. However, the experimental realizability of a steady axisymmetric bubble may also be challenged by its reachability from some initial conditions, as demonstrated by Ohta *et al.* (2005), as well as Bonometti & Magnaudet (2006), with transient simulations of initial-value problems, though restricted to axisymmetric grids. Some experiments indicated that an unstable drop may develop either oscillatory non-axisymmetric or axisymmetric behaviour (Grace, Wairegi & Brophy 1978). The growth of axisymmetric disturbances that lead to drop breakup in creeping flow was shown by experiments of Koh & Leal (1990) and by the boundary-element analysis of Pozrikidis (1990). But whether the breakup mode of bubbles at $Re \geqslant O(10)$ can be axisymmetric remains as an open question.

The author would like to thank Professor L. E. (Skip) Scriven for helpful suggestions as well as encouragement during the course of this work. Many valuable and constructive comments from Dr P. Keith Watson and the referees helped improve the quality of the presentation and therefore are highly appreciated.

REFERENCES

Batchelor, G. K. 1967 *An Introduction to Fluid Dynamics*. Cambridge University Press.

Bhaga, D. & Weber, M. E. 1981 Bubbles in viscous liquids: shapes, wakes and velocities. *J. Fluid Mech.* **105**, 61–85.

Bonometti, T. & Magnaudet, J. 2006 Transition from spherical cap to toroidal bubbles. *Phys. Fluids* **18**, 052102.

Boudouvis, A. G. 1987 Mechanisms of surface instabilities and pattern formation in ferromagnetic liquids. PhD thesis, University of Minnesota. Available from University Microfilms International, Ann Arbor, MI 48106.

Bozzi, L. A., Feng, J. Q., Scott, T. C. & Pearlstein, A. J. 1997 Steady axisymmetric motion of deformable drops falling or rising through a homoviscous fluid in a tube at intermediate Reynolds number. *J. Fluid Mech.* **336**, 1–32.

Brignell, A. S. 1973 The deformation of a liquid drop at small Reynolds number. *Q. J. Mech. Appl. Maths* **26**, 99–107.

Carvalho, M. S. 1996 Roll coating flows in rigid and deformable gaps. PhD thesis, University of Minnesota.

Chan, T. F. 1984 Newton-like pseudo-arclength methods for computing simple turning points. *SIAM J. Sci. Statist. Comput.* **5**, 135–148.

Chen, L., Garimella, S. V., Reizes, J. A. & Leonardi, E. 1999 The development of a bubble rising in a viscous liquid. *J. Fluid Mech.* **387**, 61–96.

Chen, K. S., Schunk, P. R. & Sackinger, P. A. 1995 Finite-element analyses of blade and slot coating flows using a Newton–Raphson pseudo-solid domain mapping technique and unstructured grid. In *Proc. TAPPI Coating Fundamentals Symposium*, pp. 131–152.

Christodoulou, K. N. 1989 Computational physics of slide coating flow. PhD thesis, University of Minnesota.

Christodoulou, K. N. & Scriven, L. E. 1992 Discretization of free surface flows and other moving boundary problems. *J. Comput. Phys.* **99**, 39–55.

Christov, C. I. & Volkov, P. K. 1985 Numerical investigation of the steady viscous flow past a stationary deformable bubble. *J. Fluid Mech.* **158**, 341–364.

Clift, R. C., Grace, J. R. & Weber, M. E. 1978 *Bubbles, Drops and Particles*. Academic.

Collins, R. 1966 A second approximation for velocity of a large gas bubble rising in an infinite liquid. *J. Fluid Mech.* **25**, 469–480.

Davies, R. M. & Taylor, G. I. 1950 The mechanics of large bubbles rising through extended liquids and through liquids in tubes. *Proc. R. Soc. Lond.* A **200**, 375–390.

Feng, J. Q. 1998 Computational analysis of slot coating on a tensioned web. *AIChE J.* **44**, 2137–2143.

Feng, J. Q. 2000 Contact behavior of spherical elastic particles: A computational study of particle adhesion and deformation. *Colloids Surf.* A **172**, 175–198.

Feng, J. Q. & Basaran, O. A. 1994 Shear flow over a translationally symmetric cylindrical bubble pinned on a slot in a plane wall. *J. Fluid Mech.* **275**, 351–378.

Feng, J. Q. & Scriven, L. E. 1992 Electrostatic effects in continuous liquid coating. Paper 38d in *Intl. Symposium on Coating Science and Technology. AIChE National Meeting*. New Orleans, Louisiana.

Grace, J. R., Wairegi, T. & Brophy, J. 1978 Break-up of drops and bubbles in stagnant media. *Can. J. Chem. Engng* **56**, 3–8.

Haberman, W. L. & Morton, R. K. 1953 An experimental investigation of the drag and shape of air bubbles in various liquids. *David Taylor Model Basin Rep.* 802.

Haberman, W. L. & Sayre, R. M. 1958 Motion of rigid and fluid spheres in stationary and moving liquids inside cylindrical tubes. *David Taylor Model Basin Rep.* 1143.

Harper, J. F. 1972 The motion of bubbles and drops through liquids. *Adv. Appl. Mech.* **12**, 59–129.

Hnat, J. G. & Buckmaster, J. D. 1976 Spherical cap bubbles and skirt formation. *Phys. Fluids* **19**, 182–194.

Hood, P. 1976 Frontal solution program for unsymmetric matrices. *Intl J. Numer. Meth. Engng* **10**, 379–399. (corrigendum **11**, 1055 (1977)).

Huyakorn, P. S., Taylor, C., Lee, R. L. & Gresho, P. M. 1978 A comparison of various mixed interpolation finite elements in the velocity–pressure formulation of the Navier–Stokes equations. *Comput. Fluids* **6**, 25–35.

Iooss, G. & Joseph, D. D. 1990 *Elementary Stability and Bifurcation Theory*, 2nd edn. Springer.

Joseph, D. D. 2003 Rise velocity of a spherical-cap bubble. *J. Fluid Mech.* **488**, 213–223.

KELLER, H. B. 1977 Numerical solution of bifurcation and nonlinear eigenvalue problems. In *Applications of Bifurcation Theory* (ed. P. H. Rabinovich), pp. 359–384. Academic.

KOH, C. J. & LEAL, L. G. 1990 An experimental investigation on the stability of viscous drops translating through a quiescent fluid. *Phys. Fluids* A **2**, 2103–2109.

LEVICH, V. G. 1962 *Physicochemical Hydrodynamics*. Prentice-Hall.

LEVICH, V. G. & KRYLOV, V. S. 1969 Surface-tension-driven phenomena. *Annu. Rev. Fluid Mech.* **1**, 293–316.

MIKSIS, M. J., VANDEN-BROECK, J.-M. & KELLER, J. B. 1981 Axisymmetric bubble or drop in a uniform flow. *J. Fluid Mech.* **108**, 89–100.

MIKSIS, M. J., VANDEN-BROECK, J.-M. & KELLER, J. B. 1982 Rising bubbles. *J. Fluid Mech.* **123**, 31–41.

MOORE, D. W. 1959 The rise of a gas bubble in a viscous liquid. *J. Fluid Mech.* **6**, 113–130.

MOORE, D. W. 1965 The velocity of rise of distorted gas bubbles in a liquid of small viscosity. *J. Fluid Mech.* **23**, 749–766.

MUSSON, L. C. 2001 Two-layer slot coating. PhD thesis, University of Minnesota.

OHTA, M., IMURA, T., YOSHIDA, Y. & SUSSMAN, M. 2005 A computational study of the effect of initial bubble condition on the motion of a gas bubble rising in viscous liquids. *Intl J. Multiphase Flow* **31**, 223–237.

ORTEGA, J. M. & RHEINBOLDT, W. C. 1970 *Iterative Solution of Nonlinear Equations in Several Variables*. Academic.

PARLANGE, J. Y. 1969 Spherical-cap bubbles with laminar wakes. *J. Fluid Mech.* **37**, 257–263.

POZRIKIDIS, C. 1990 The instability of a moving viscous drop. *J. Fluid Mech.* **210**, 1–21.

RIKS, R. 1972 The application of Newton's method to the problem of elastic stability. *J. Appl. Mech.* **39**, 1060–1065.

RYSKIN, G. & LEAL, L. G. 1984 Numerical solution of free-boundary problems in fluid mechanics. Part 2. Buoyancy-driven motion of a gas bubble through a quiescent liquid. *J. Fluid Mech.* **148**, 19–35.

SACKINGER, P. A., SCHUNK, P. R. & RAO, R. R. 1996 A Newton–Raphson pseudo-solid domain mapping technique for free and moving boundary problems: A finite element implementation. *J. Comput. Phys.* **125**, 83–103.

DE SANTOS, J. M. 1991 Two-phase cocurrent downflow through constricted passages. PhD thesis, University of Minnesota.

SLAUGHTER, I. & WRAITH, A. E. 1968 The wake of a large gas bubble. *Chem. Eng. Sci.* **23**, 932.

STEWART, G. W. 1981 On the implicit deflation of nearly singular systems of linear equations. *SIAM J. Sci. Statist. Comput.* **2**, 136–140.

STRANG, G. & FIX, G. J. 1973 *An Analysis of the Finite Element Method*. Prentice-Hall.

SUGIYAMA, K., TAKAGI, S. & MATSUMOTO, Y. 2001 Multi-scale analysis of bubbly flows. *Comput. Methods Appl. Mech. Engng* **191**, 689–704.

TAYLOR, T. D. & ACRIVOS, A. 1964 On the deformation and drag of a falling viscous drop at low Reynolds number. *J. Fluid Mech.* **18**, 166–176.

THOMPSON, J. F., WARSI, Z. U. A. & MASTIN, C. W. 1985 *Numerical Grid Generation*. Elsevier.

TRYGGVASON, G., BUNNER, B. ESMAEELI, A., JURIC, D. AL-RAWAHI, N., TAUBER, W., HAN, J., NAS, S. & JAN, Y.-J. 2001 A front-tracking method for the computations of multiphase flow. *J. Comput. Phys.* **169**, 708–759.

VAN DYKE, M. 1975 *Perturbation Methods in Fluid Mechanics*. The Parabolic Press.

WEGENER, P. P. & PARLANGE, J.-Y. 1973 Spherical-cap bubbles. *Annu. Rev. Fluid Mech.* **5**, 79–100.